An Axial Airgap Eddy Current Speed Sensor

Mehran Mirzaei, Pavel Ripka and Vaclav Grim

Abstract—**This paper presents a novel configuration of the eddy current speed sensor to measure the rotating speed of iron rods and shafts up to 3000 rpm. The proposed eddy current speed sensor has an axial airgap structure with one excitation coil and two antiserially connected pick up coils. The speed sensor is mounted in the end shaft part region. Different solid iron materials for rotating shaft are considered in the measurements and calculations to evaluate solid iron material effect on the eddy current speed sensor performance. 2D and 3D finite element method is utilized for the performance analysis of the speed sensor. Also a 2D analytical method is developed for parametric analysis. A copper rod is also used to compare the speed sensor with the rotating iron shaft and copper shaft. Finally, two thin copper discs with different diameters are mounted on the solid iron shaft and their influences on the eddy current speed sensor were evaluated and measured to increase sensitivity and decrease sensor dependency on the permeability of the solid iron shaft. The achieved nonlinearity errors are about ±0.2%.**

Index Terms—**Axial airgap, eddy current, speed sensor, 2D and 3D FEM, analytical, material effects.**

I. INTRODUCTION

SPEED measurement is a key theme in the control, protection, and maintenance of rotating machinery. As industry electrification for rotating machinery is growing, fast and robust measurements of rotating speed are vital. The compactness of the sensor and system for speed measurement is also essential, especially for short axial length electrical machines [1]-[5] as the speed sensor is mounted on the non-drive end of machines. Many speed sensors are based on optical principles. Nonintrusive reflective sensor for the ultra-high-speed switched reluctance machines is described in [6]. Optical sensors are susceptible to dust and grease so that they are not ideal for a harsh environment.

The triboelectric effect was utilized in [7] to measure speed, which is sensitive to dust and dirt because of electrostatic phenomena. The sensorless method was investigated and used for speed estimation [8], however, it is less reliable in faulty conditions.

Magnetic speed sensors are robust, cheap, and reliable. An absolute magnetic rotary sensor suitable for the measurement of the angular position of motors was proposed in [9]. The sensor consists of five flat coils: the large excitation coil and four symmetrical receiving coils. The field in the receiving coils depends on the position of the conducting strip. The sensor is only 4.5 mm thick. However, this principle requires a shaft with salient conductivity.

M. Mirzaei, P. Ripka and V. Grim are with faculty of electrical engineering, Czech Technical University, Prague, 16627, Czech Republic (email: mirzameh@fel.cvut.cz).

A resolver is a long-established analog transducer for the position and speed measurement without electronics processing [10]-[12]. The conventional model of resolver has rotor winding and two stationary perpendicular windings on the stator creating a rotating field. Resolver has a similar performance as a rotating transformer. The rotor winding needs moving contacts which makes it less reliable at higher speeds. Rotor winding can be replaced with a salient shape iron rotor as an alternative. This is a kind of variable reluctance sensor [13] and [14]. Rotating encoder or digital resolver for speed measurement is a transducer with digital outputs. The disadvantage of the resolvers is that they occupy considerable space at the non-drive part of the housing. Also, resolvers can be less practical at higher speeds as a sensitive rotating part is on the shaft. A contactless speed sensor using moving permanent magnets was presented in [15], which is based on eddy current coupling [16], has the drawback of having a mechanical moving part. References [17] and [18] presented speed measurements utilizing stray flux in electrical machines inside the housing and end winding or on the external surface of the housing, which are not enough fault tolerant especially to overheating and mechanical fault.

Utilizing the motional component of induced eddy current in smooth conductive objects has been presented in numerous papers. As an example, the early works on speed measurement of fluids or flowmeters were presented in [19] and [20] using contact electrode or pick up coils to measure the voltage, which is proportional to the fluid speed. Later linear eddy current speed measurements for solid moving objects were developed and presented in [21]-[24] for nonmagnetic materials, which speed estimation was performed using induced voltage in the pick up coils or measured magnetic fields using, for example, Hall sensor. Eddy current speed sensors for rotating speed measurement were presented by authors in [25]-[26] with pick up coils for voltage measurement and cylindrical structure, which could be less efficient to utilize in the disc shape and axial airgap machines [27]. These types of machines are designed to have very short axial length (such as Pancake shape with large diameter to axial length ratio) for industrial applications with axial length constraint [28]. Therefore, axial airgap eddy current speed sensor is preferable as it has shorter axial length.

In this paper, a disc shape configuration of eddy current speed sensor with axial airgap and compact axial length is measured up to 3000 rpm and analyzed using approximate 2D analytical method and 2D and 3D time stepping finite element method (FEM). The sensor comprises one excitation coil and two antiserially connected pick up coils, which are shielded by thin disc steel lamination. The sensor can be installed in the

non-drive end part of a machine shaft. The measurements and analyses are performed at various constant speeds and different excitation frequencies. The sensitivity and linearity characteristics of the sensor and the material effect of the solid iron shaft on the sensor performance are investigated.

II. MODEL

Table I and Fig. 1 present an axial air gap sensor with a rotating conductive shaft and its dimensional parameters. The sensor has one excitation coil and two antiserially connected pick up coils. It has a magnetic shield or yoke, which is a disc shape silicon steel lamination in this paper. The outer diameter of the magnetic shield is the same outer diameter of a rotating copper or iron shaft.

The eddy current speed sensor utilizes a motional component of induced eddy current caused by a rotating conductive shaft. The motional component of induced eddy current makes asymmetrical magnetic flux distribution in double sides of the excitation coil as shown in Fig. 2. The asymmetrical flux distribution induces a nonzero voltage on antiserially connected pick up coils. Fig. 3 and Fig. 4 present induced voltages of each pick up coil and resultant differential voltage of antiserially connected pick up coils versus speed at 1.6 mm magnetic gap between coils and rotating shaft using the analytical method in Appendix.

TABLE I
PARAMETERS OF EDDY CURRENT SPEED SENSOR

| Parameter	Definition	Value
N_e	Number of turns in the excitation coil	1000
N_p	Number of turns in the pick up coils	1000
r_o	The outer radius of the rotating shaft	15 mm
r_d	The outer radius of the copper disc	15 and 25 mm
r_m	Mean radius of coils	10 mm
g_m	The gap between coils and shaft	1.6 and 2.6 mm
g_s	The gap between coils and shield	1.6 mm
h_c	Coil height in the axial direction	5 mm
h_d	Copper disc thickness	0.6 mm
h_s	Shield thickness	0.5 mm
t_c	Coil thickness in azimuthal direction	1.2 mm
w_c	Coil sides distance	13.8 mm
L_r	Length of the straight part of the coil	10 mm
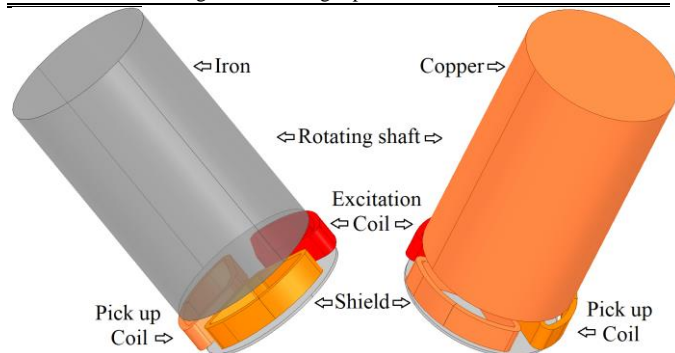
Fig. 1. Axial airgap eddy current speed sensor with shield and magnetic yoke with rotating iron shaft and with rotating copper shaft
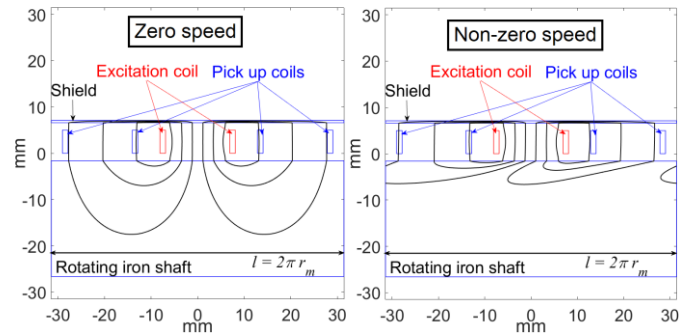

Fig. 2. Schematic flux distribution in the linearized model of axial airgap eddy current speed sensor at zero speed (magnetic flux is symmetric) and nonzero speed (magnetic flux is asymmetric).
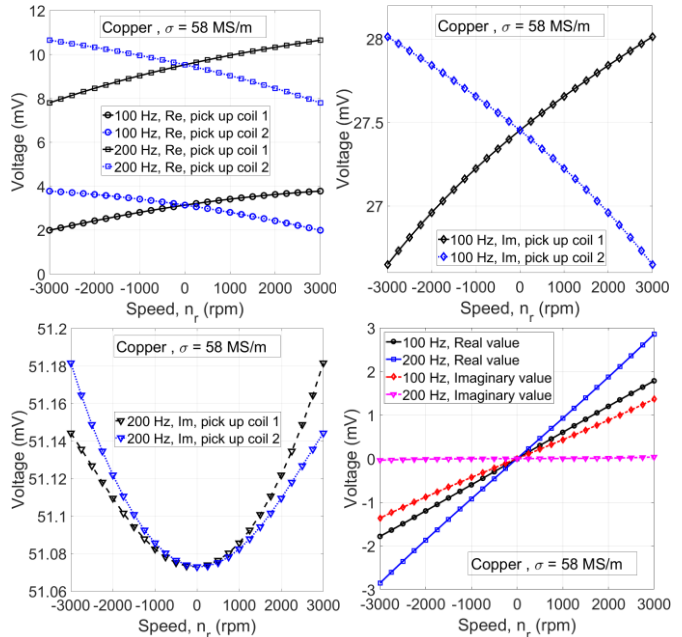

Fig. 3. Real (Re) and imaginary (Im) components of Induced voltage of individual pick up coils and antiserailly connected pick up coils versus speed for rotating copper shaft – analytical method in Appendix
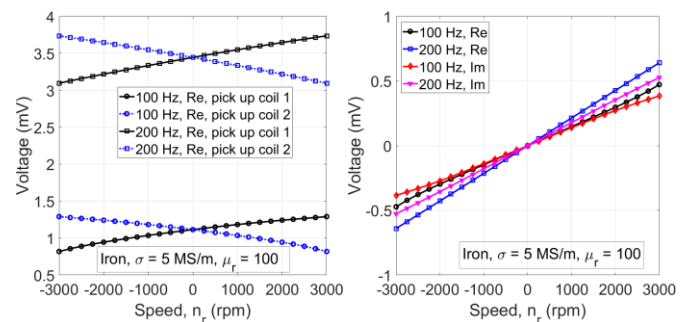

Fig. 4. Real (Re) component of Induced voltage of individual pick up coils (left) and antiserially connected pick up coils (right) versus speed for rotating iron shaft - analytical method in Appendix

RMS value of excitation current is considered 15.5 mA in the analytical calculations. Induced voltages of each pick up coil decrease or increase versus speed depending on the speed direction of the shaft as shown in Fig. 3 and Fig. 4. Therefore, the differential voltage of antiserially connected pick up coils 1 and 2 is proportional to the speed value and direction. The real component (Re) and imaginary component (Im) of induced voltages are considered relative to excitation coil current as a

reference signal. The real component of the voltage induced into the pick up coils voltage (1 and 2) is smaller than the imaginary component of voltage at 100 Hz and 200 Hz but it increases or decreases with higher slope versus speed.

III. PARAMETRIC ANALYSIS

Induced voltages of antiserially connected pick up coils versus frequency show different trends for copper and iron rotating shafts as shown in Fig. 5. For example, the real component of voltage versus frequency increases according to the induction law and then decreases for copper shaft, but it increases monotonically for iron shaft due to its lower conductivity and higher permeability.

The material of the magnetic and nonmagnetic rotating shaft could be changed for various applications or its properties varies by temperature. Shaft Material effects are evaluated in Fig. 6 and Fig. 7. The maximum value of induced voltage for nonmagnetic shaft shifts to lower conductivities at higher frequencies. Because skin depth and flux penetration are higher with lower conductivity, which induced voltage becomes higher (Fig. 6). The graphs of induced voltage for the magnetic iron shaft in Fig. 7 show that real and imaginary components of induced voltages increase with increasing conductivity and decreasing relative magnetic permeability for real and imaginary components of induced voltage at 100 Hz and 200 Hz. Adding copper disc on shaft end surface as shown in Fig. 8 increases sensitivity of eddy current speed sensor in comparison with an only iron rotating shaft (Fig. 9).
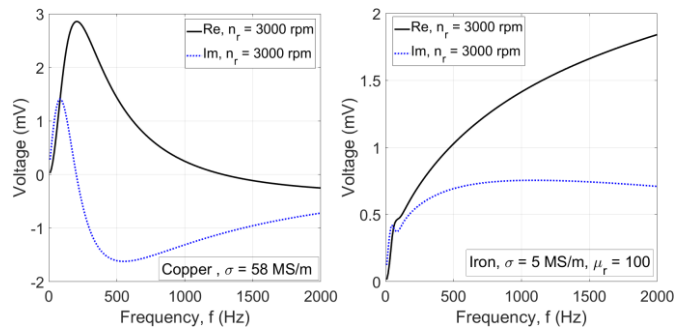

Fig. 7. Real (Re) and imaginary (Im) components of the induced voltage of antiserially connected pick up coils for an only rotating iron shaft versus electrical conductivity and relative magnetic permeability – analytical method in Appendix

Fig. 8. Axial airgap eddy current speed sensor with shield and magnetic yoke with rotating iron shaft with 3 cm and 5 cm copper disc.

Fig. 5. Real (Re) and imaginary (Im) components of the resultant induced voltage of antiserailly connected pick up coils for the copper shaft (left) and for the iron shaft (right) versus frequency – analytical method in Appendix

Fig. 9. Real (Re) component of Induced voltage of individual pick up coils and antiserially connected pick up coils for rotating iron shaft with 3 cm diameter copper disc – analytical method in Appendix
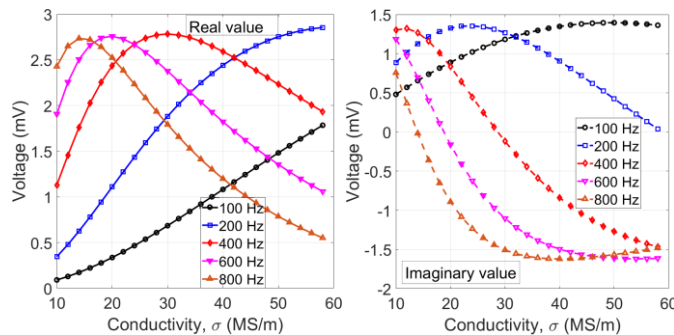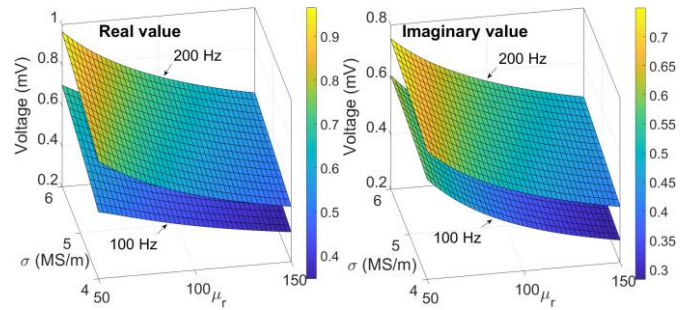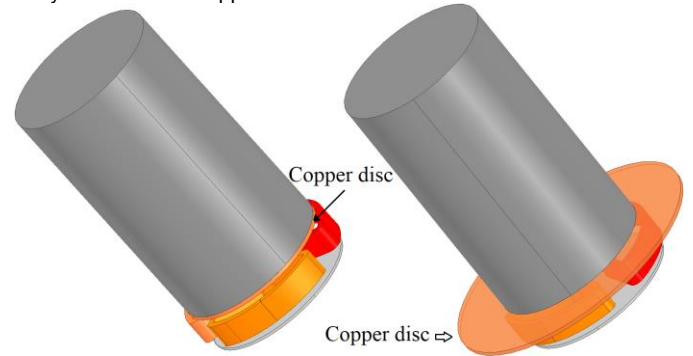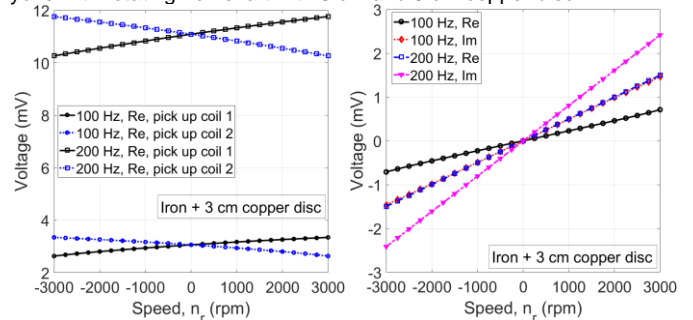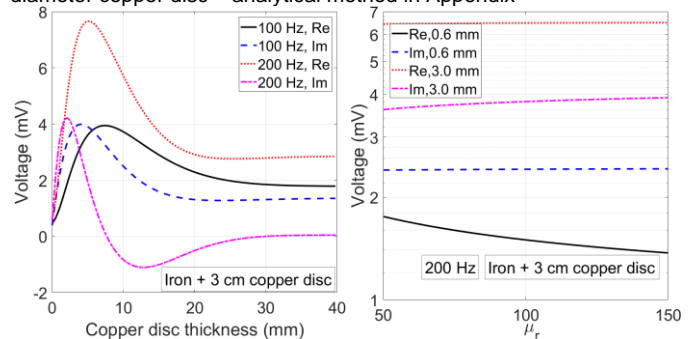

Fig. 6. Real (Re) and imaginary (Im) components of Induced voltage of antiserially connected pick up coils versus electrical conductivity for rotating nonmagnetic shaft - analytical method in Appendix

Fig. 10. Real (Re) and imaginary (Im) components of the induced voltage of antiserially connected the pick up coils for rotating iron shaft with 3 cm diameter copper disc a) versus copper disc thickness (left) and b) versus relative magnetic permeability of rotating iron for different copper disc thickness, 0.6 mm and 3.0 mm (right) - analytical method in Appendix

Influences of copper disc thickness on induced voltage in Fig. 10 a), show that optimum selection of copper thickness can considerably increase the induced voltage. Copper disc minimizes the effect of relative magnetic permeability

variations of the iron shaft on the induced voltage of the speed sensor as shown in Fig. 10 b), which an advantage to compensate rotating shaft materials effects on the speed sensor performance.

IV. EXPERIMENTAL RESULTS

Fig. 11 shows the rotating copper shaft and eddy current sensor. The voltage of pick up coils is measured using a lock-in amplifier. Fig. 12 presents a schematic block diagram of a lock-in amplifier. Real and imaginary components of voltage are measured relative to the excitation coil current as a reference signal. Three different solid irons are used for rotating iron shafts with different conductivities and relative magnetic permeabilities (Table II). The conductivities were measured and the relative magnetic permeabilities were estimated using FEM and measurements. The measurements are performed with a magnetic gap of 1.6 mm and 2.6 mm at 100 Hz, 200 Hz, 400 Hz, 600 Hz, and 800 Hz.

The real and imaginary components of measured voltage for the copper shaft in Fig. 13 are satisfactory linear curves, however, only the real component of measured voltage for the iron shaft is an acceptable linear curve. The real component of induced voltage or sensitivity of speed sensor increases with increasing frequency in the iron shaft; however, it decreases for copper shaft at higher frequencies above 200 Hz.

Fig. 11. Experimental elements– with rotating copper shaft and axial airgap eddy current speed sensor
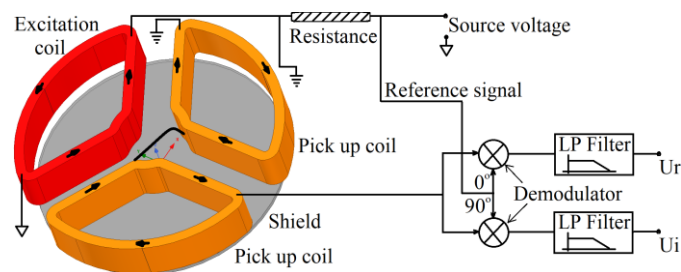

Fig. 12. Schematic block diagram of the lock-in amplifier

TABLE II
MATERIAL PROPERTIES OF ROTATING SHAFT

Material	Magnetic relative permeability, μ_r	Conductivity, σ_i (MS/m)
Iron 1	86.57	5.39
Iron 2	88.83	5.24
Iron 3	78.35	4.29
Copper	1	58

Fig. 13. Real (Re) and imaginary (Im) components of the induced voltage of antiserially connected pick up coils for rotating copper shaft - Experimental

Fig. 14. Real (Re) and imaginary (Im) components of the induced voltage of antiserially connected pick up coils for only rotating iron shaft - Experimental

Fig. 15. Experimental elements with DC motor as a prime mover– with iron and copper disc shaft and axial airgap eddy current speed sensor
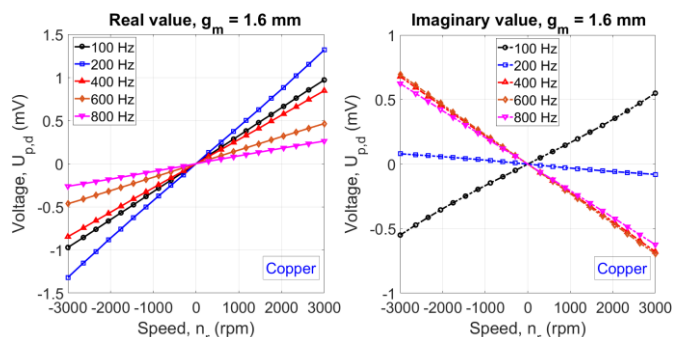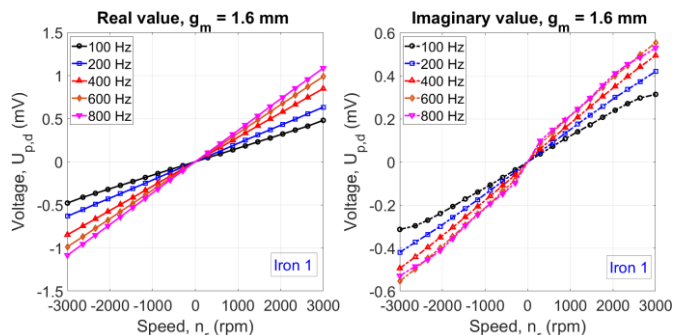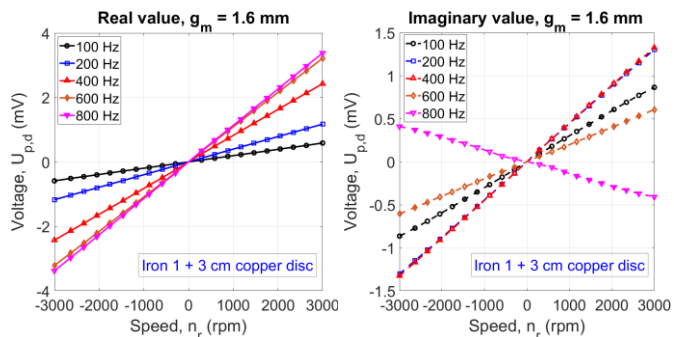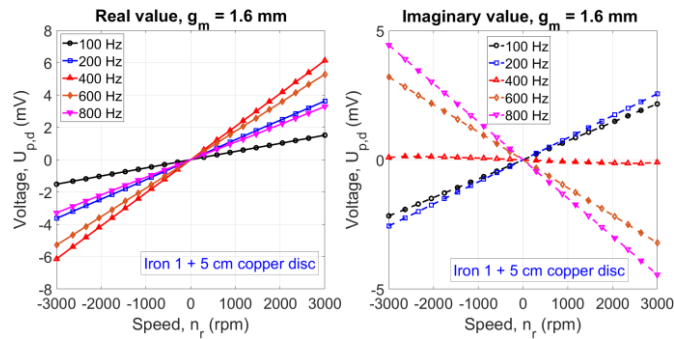
Fig. 16. Real (Re) and imaginary (Im) components of the induced voltage of antiserially connected pick up coils for rotating iron shaft with 0.6 mm thick and 3 cm (up) and 5 cm (bottom) diameter copper disc - Experimental

The experimental structures of rotating iron shafts with the copper disc are shown in Fig. 15. Copper discs with a thickness of 0.6 mm and diameters of 3 cm and 5 cm are used for the measurements (Fig. 8). Adding copper disc to rotating iron shaft increases sensitivity of eddy current speed sensor in Fig. 16. The induced voltages are considerably higher with a 5 cm diameter copper disc in comparison with a 3 cm diameter copper disc because a larger-diameter disc has higher equivalent conductivity and lower resistance to the induced eddy currents.

The sensor voltage is linearly proportional to the excitation coil current and therefore, the sensor accuracy depends on the excitation current. The excitation coil is connected to a constant voltage source with 10 V amplitude and internal resistance 50 Ω. A 10 Ω resistance is used in series with the excitation coil to measure the excitation current as shown in Fig. 12. The measured currents decrease with frequency frequency as shown in Fig. 17. It decreases by about 5% from 100 Hz to 800 Hz because of increasing excitation coil reactance.
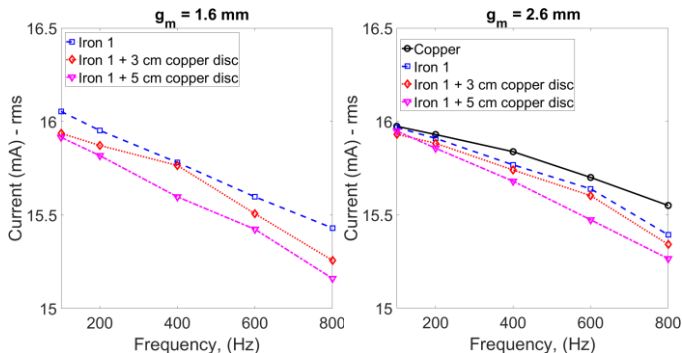

Fig. 17. The excitation coil current versus frequency for g_m=1.6 mm (left) and g_m=2.6 mm (right) – Experimental results

Table III and Table IV present sensitivity coefficients, K_R and K_I (mV/rpm) of real and imaginary components of differential voltage ($U_{p,d-R}$ and $U_{p,d-I}$) of antiserially connected pick up coils at 100 Hz, 200 Hz, 400 Hz, 600 Hz, and 800 Hz versus rotational speed, n_r:

$$U_{p,d-R} = K_R \cdot n_r, \qquad U_{p,d-I} = K_I \cdot n_r$$
(1)

Increasing magnetic gap, g_m about 63% in percentage from

1.6 mm to 2.6 mm has less change in induced voltage than 63% in percentage, for example, less than 25% in the iron shaft with and without copper disc. Higher airgap has a mechanical advantage in terms of less mechanical tolerance and complexity for mounting eddy current speed sensor, especially at higher speeds operation.

Differences between induced voltages and sensitivities in Table III and Table IV for iron 1 with copper disc and iron 3 with the copper disc are lower compared to the corresponding values for iron shaft without copper disc as the induced voltages are less dependent on material conductivity and relative magnetic permeability of iron shaft as shown in Fig. 10. The copper disc with 5 cm diameter suppresses the effects of iron shaft materials more than copper disc with 3 cm diameter due to the stronger induced eddy current and its higher reaction fields. Copper disc with 5 cm diameter has less edge effects in comparison with copper disc with 3 cm diameter and higher effective conductivity according to Russel-Northworthy factor, k_{R-N}, (see (5) in Appendix). This factor for first harmonic ($n=\pm1$) is calculated 0.157 for 3 cm disc and it is 0.467 for 5 cm disc.

TABLE III
SENSITIVITY COEFFICIENT, K_R FOR REAL COMPONENT OF VOLTAGE

Frequency (Hz)		100	200	400	600	800
Iron 1+	g_m=1.6 mm	20e-5	39e-5	81e-5	108e-5	113e-5
3 cm copper	g_m=2.6 mm	16e-5	32e-5	67e-5	93e-5	100e-5
Iron 1+	g_m=1.6 mm	51e-5	122e-5	205e-5	176e-5	109e-5
5 cm copper	g_m=2.6 mm	38e-5	94e-5	165e-5	153e-5	106e-5
Iron 3+	g_m=1.6 mm	19e-5	41e-5	85e-5	112e-5	116e-5
3 cm copper	g_m=2.6 mm	14e-5	30e-5	64e-5	88e-5	96e-5
Iron 3+	g_m=1.6 mm	50e-5	126e-5	211e-5	177e-5	105e-5
5 cm copper	g_m=2.6 mm	38e-5	97e-5	169e-5	166e-5	109e-5
Iron 1	g_m=1.6 mm	16e-5	21e-5	28e-5	33e-5	36e-5
	g_m=2.6 mm	12e-5	17e-5	22e-5	26e-5	29e-5
Iron 2	g_m=1.6 mm	14e-5	19e-5	26e-5	31e-5	34e-5
	g_m=2.6 mm	11e-5	15e-5	21e-5	24e-5	27e-5
Iron 3	g_m=1.6 mm	13e-5	18e-5	24e-5	29e-5	32e-5
	g_m=2.6 mm	10e-5	14e-5	20e-5	23e-5	25e-5
Copper	g_m=1.6 mm	32e-5	43e-5	28e-5	16e-5	8.9e-5
	g_m=2.6 mm	25e-5	34e-5	27e-5	19e-5	14e-5

TABLE IV
SENSITIVITY COEFFICIENT, K_I FOR IMAGINARY COMPONENT OF VOLTAGE

Frequency (Hz)		100	200	400	600	800
Iron 1+3 cm	g_m=1.6 mm	29e-5	44e-5	44e-5	20e-5	-14e-5
copper	g_m=2.6 mm	25e-5	38e-5	42e-5	24e-5	0
Iron 1+	g_m=1.6 mm	73e-5	85e-5	-5.1e-5	-107e-5	-148e-5
5 cm copper	g_m=2.6 mm	59e-5	73e-5	9.7e-5	-67e-5	-105e-5
Iron 3+	g_m=1.6 mm	31e-5	46e-5	45e-5	16e-5	-18e-5
3 cm copper	g_m=2.6 mm	25e-5	38e-5	41e-5	24e-5	0
Iron 3+	g_m=1.6 mm	75e-5	88e-5	-10.4e-5	-111e-5	-153e-5
5 cm copper	g_m=2.6 mm	61e-5	75e-5	11e-5	-68e-5	-105e-5
Iron 1	g_m=1.6 mm	11e-5	14e-5	17e-5	19e-5	19e-5
	g_m=2.6 mm	9.2e-5	12e-5	14e-5	15e-5	15e-5
Iron 2	g_m=1.6 mm	11e-5	14e-5	17e-5	19e-5	20e-5
	g_m=2.6 mm	8.7e-5	11e-5	14e-5	15e-5	15e-5
Iron 3	g_m=1.6 mm	10e-5	13e-5	16e-5	17e-5	17e-5
	g_m=2.6 mm	8.5e-5	11e-5	13e-5	14e-5	14e-5
Copper	g_m=1.6 mm	18e-5	-2.8e-5	-22e-5	-23e-5	-21e-5
	g_m=2.6 mm	15e-5	1.9e-5	-12e-5	-15e-5	-14e-5

3D FEM analyses (Fig. 18) at 100 Hz and 200 Hz for 1171.9 rpm and 3000 rpm are performed for comparison with measurements. The simulation results coincide well with

measured results concerning rotor material effects on speed sensor performance (Table V – Table VIII). The mismatch between 3D FEM and measurements is mainly caused by inexact material data especially relative magnetic permeability for the iron of shaft and a larger gap in measurements, which cause 3D FEM results to become higher than measurements.

Time stepping FEM with consideration of movement is used for the simulation of axial airgap eddy current speed sensor to model shaft motion and induced eddy currents in the rotating conductive shaft [29]-[30]. Multiple connected conductive regions can be considered in the simulations using this method.
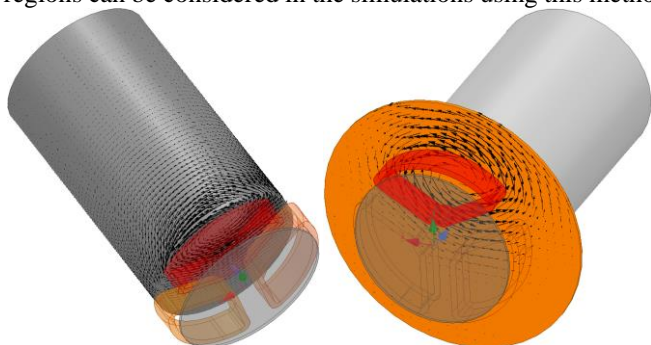

Fig. 18. Eddy current distribution on a rotating shaft, a) an only iron (left) and b) with a copper disc (right) – 100 Hz and 3000 rpm

TABLE V
COMPARISON BETWEEN EXPERIMENTAL AND FEM RESULTS

g_{m} = 1.6 mm 1171.9 rpm		$U_{\mathrm{p,d}}$ (mV) at 100 Hz		$U_{\mathrm{p,d}}$ (mV) at 100 Hz	
		3D FEM	Exp.	3D FEM	Exp.
Iron	Iron 1	0.4743	0.4185	0.7698	0.6961
+3 cm copper	Iron 3	0.4678	0.4234	0.7701	0.7225
Iron	Iron 1	1.2124	1.049	1.94	1.757
+5cm copper	Iron 3	1.2076	1.062	1.9616	1.819
Iron 1		0.2413	0.2304	0.3048	0.3045
Iron 2		0.2338	0.2088	0.2970	0.2826
Iron 3		0.2280	0.1962	0.2899	0.2626
Copper		0.4562	0.4276	0.4976	0.5028

TABLE VI
COMPARISON BETWEEN EXPERIMENTAL AND FEM RESULTS

g_{m} = 1.6 mm 3000 rpm		$U_{\mathrm{p,d}}$ (mV) at 100 Hz		$U_{\mathrm{p,d}}$ (mV) at 200 Hz	
		3D FEM	Exp.	3D FEM	Exp.
Iron	Iron 1	1.2326	1.046	1.9602	1.754
+3 cm copper	Iron 3	1.2253	1.074	1.9467	1.83
Iron	Iron 1	3.1057	2.644	4.9995	4.439
+5cm copper	Iron 3	3.1030	2.686	5.0928	4.594
Iron 1		0.6645	0.573	0.8099	0.7591
Iron 2		0.6461	0.5045	0.7842	0.7017
Iron 3		0.6380	0.4938	0.7694	0.6587
Copper		1.1915	1.116	1.3352	1.322

TABLE VII
COMPARISON BETWEEN EXPERIMENTAL AND FEM RESULTS

g_{m} = 2.6 mm 1171.9 rpm		$U_{\mathrm{p,d}}$ (mV) at 100 Hz		$U_{\mathrm{p,d}}$ (mV) at 200 Hz	
		3D FEM	Exp.	3D FEM	Exp.
Iron	Iron 1	0.3733	0.3499	0.6079	0.5899
+3 cm copper	Iron 3	0.3692	0.338	0.6061	0.5673
Iron	Iron 1	0.8913	0.8279	1.4905	1.409
+5 cm copper	Iron 3	0.8901	0.8467	1.5077	1.444
Iron 1		0.1784	0.1815	0.2459	0.2408
Iron 2		0.1758	0.1669	0.2405	0.2242
Iron3		0.1708	0.1576	0.2330	0.2111
Copper		0.3552	0.3363	0.4162	0.4004

TABLE VIII
COMPARISON BETWEEN EXPERIMENTAL AND FEM RESULTS

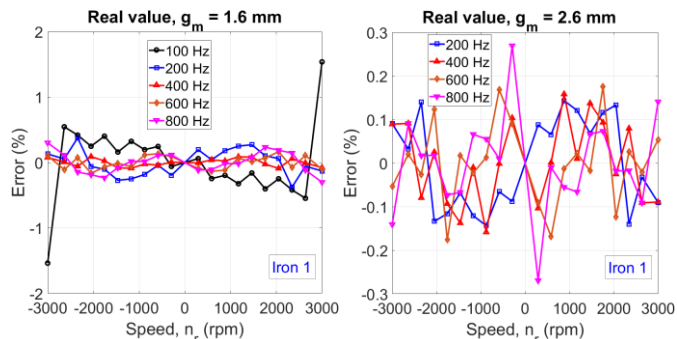| g_{m} = 2.6 mm 3000 rpm		$U_{\mathrm{p,d}}$ (mV) at 100 Hz		$U_{\mathrm{p,d}}$ (mV) at 200 Hz	
		3D FEM	Exp.	3D FEM	Exp.
Iron	Iron 1	0.9712	0.8833	1.5527	1.489
+3 cm copper	Iron 3	0.966	0.8533	1.5484	1.438
Iron	Iron 1	2.3768	2.107	3.8656	3.561
+5 cm copper	Iron 3	2.3793	2.138	3.9097	3.671
Iron 1		0.5033	0.458	0.6207	0.6044
Iron 2		0.4915	0.4104	0.6073	0.5622
Iron3		0.4826	0.4005	0.5940	0.5303
Copper		0.9401	0.8724	1.0910	1.04

Fig. 19. Nonlinearity errors versus speed for an only rotating iron shaft at 1.6 mm and 2.6 mm magnetic gap between coils and rotating shaft - Experimental
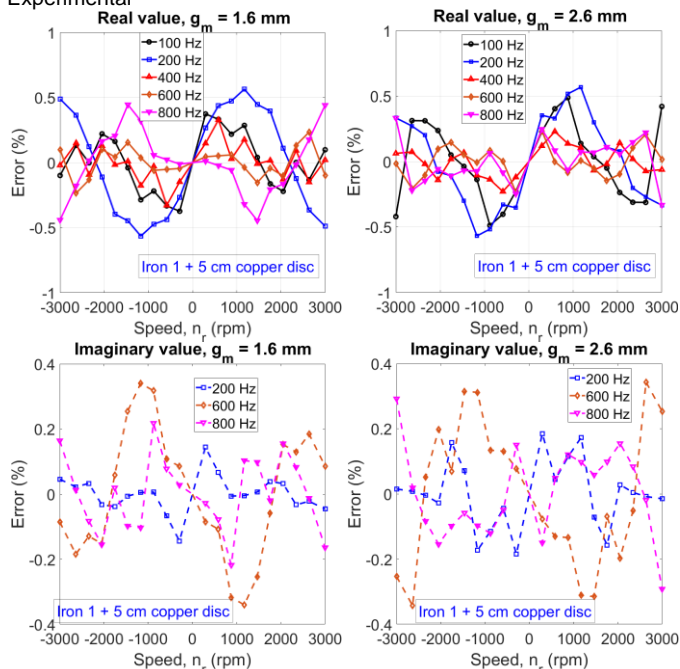

Fig. 20. Nonlinearity errors versus speed for rotating iron shaft with the copper disc at 1.6 mm and 2.6 magnetic gap between coils and rotating shaft and disc - Experimental

V. NONLINEARITY ERROR ANALYSIS

The nonlinearity error is expressed in percentage of the full scale. Nonlinearity errors of the measured induced voltage of antiserially connected pick up coils are shown in Fig. 18 and Fig. 19 for an only iron shaft and iron shaft with the copper disc at different frequencies and the magnetic gap between coils and rotating part. The nonlinearity errors are quite low as 0.2%.

The main noninherent or external reason for nonlinearity could be due to the imperfect flatness of the end shaft surface. For example, nonuniformity of the end shaft surface (see Fig.

24) was modeled using 2D FEM with 0.5 mm saliency and the results are shown in Fig. 21 at 600 rpm and 200 Hz. The frequency spectrum of the induced voltage consists of main frequency, 200 Hz and two side frequencies, 200±10 Hz, where 10 Hz is frequency corresponding to rotation speed. The parasitic signal at side frequencies cannot be efficiently suppressed by the filter in the lock in amplifier and contribute to linearity errors.
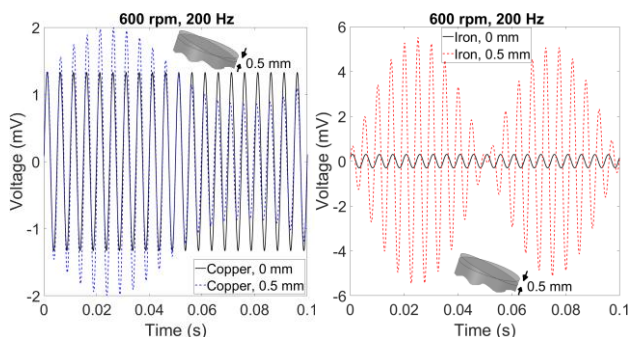

Fig. 21. The induced voltage of antiserially connected pick up coils for rotating copper shaft and iron shaft – 2D FEM using linearized model. Flat shaft and shaft with 0.5 mm saliency are considered

VI. HIGH SPEED OPERATION

Fig. 22 shows simulations of axial airgap eddy current speed sensor for higher speed range, ±30000 rpm. The excitation frequency should be increased to obtain appropriate linearity for the sensor operation. For example, excitation frequency, 2000 Hz provides satisfactory results in Fig. 22 for speed range ±30000 rpm. The sensor does not have an upper speed limitation.
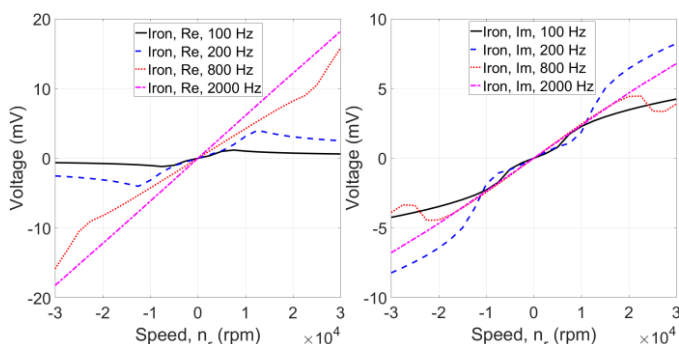

Fig. 22. Real (Re) and imaginary (Im) components of the induced voltage of antiserially connected pick up coils for rotating iron shaft up to ± 30000 rpm - analytical method in Appendix with I = 15.5 mA

VII. DISCUSSIONS

Using the fluxgate effect in an amorphous ring core to measure the field of motional component of induced eddy currents was presented in [31] for a speed sensor. This sensor has a high nonlinearity error of approximately 5% and complicated structure. A Hall sensor for speed measurement using permanent magnet excitation and utilizing motional component of induced eddy currents was presented in [32] with poor offset stability and high nonlinearity error. The proposed axial airgap eddy current speed sensor in this paper has 0.2% nonlinearity error, which is better than industrial tachometer

with 1.0% nonlinearity error [33]. The proposed eddy current sensor in this paper has significant advantages: it has low nonlinearity error, it is cost effective cost effective and compact.

A commercial lock-in amplifier chip could be used if a real or imaginary component of induced voltage is desired for the speed meter depending on their superiority in terms of higher linearity and sensitivity. However, a simple rms reader can be used for speed measurement when real and imaginary components of induced voltage curve versus speed are a satisfactory straight line.

Compensating effects of shaft material, temperature, and varying mechanical and magnetic gaps between sensor and rotating shaft are important for industrial speed sensor design. Pulsed eddy current method and multi-frequency method [34] are well known contactless and nondestructive approaches to compensate gap variation or liftoff, which can be utilized also for the eddy current speed sensor. Using signal with square, triangle, and sawtooth waveforms is another option. The amplitude and phase of the harmonic components in the induced voltage could be used for the compensation too. Another advantage of measuring real and imaginary components of voltage is that one can be used for speed meter and another one can be considered for compensation purpose if both components are adequate straight line versus speed. Another possible compensation method is ratiometric processing, $(U_{p,l}-U_{p,r})/(U_{p,l}+U_{p,r})$ of the pickup voltages, which is successfully utilized in LVDT sensors. For example, Fig. 23 shows the effect of increasing of gap between coils and rotating part, g about 25% (1.6 mm to 2 mm). Real component of induced voltage decreases 7.65%. However, corresponding ratiometric value changes by only 2.8%.
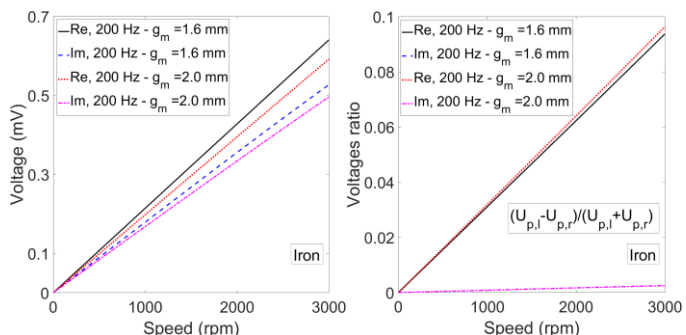

Fig. 23. Real (Re) and imaginary (Im) components of Induced voltage of antiserially connected pick up coils versus speed for rotating iron shaft (left) and ratiometric outputs (right) - analytical method in Appendix

The proposed eddy current speed sensor can be utilized for speed range ±3000 rpm in all industrial applications using standard rotating electrical and mechanical machines, for examples, squirrel cage induction machines. Therefore, this sensor is suitable for most standard applications, include fans, pumps, grinders, conveyors, mills, crushers, agitators, positioners, roller and gate drives, and other applications.

Decreasing diameter of shaft reduces output voltage and sensitivity of the sensor as the sensitivity is dependent on the shaft diameter. Attaching larger magnetic (iron) or nonmagnetic (brass, aluminum or copper) diameter disc to the

shaft as shown in Fig. 8 or increasing excitation frequency are techniques to keep sensitivity at proper value for smaller shafts.

VIII. CONCLUSION

A novel axial airgap eddy current sensor was presented, and its performance was measured and analyzed with consideration of electrical and magnetic properties and mechanical parameters. The proposed eddy current speed sensor is simple, cost-effective, and compact with excellent linearity, which shows its high potentiality for industrial applications. The measured nonlinearity error is as low as ±0.2%. Using a copper disc with an iron rotating shaft causes higher sensitivity and lower nonlinearity error in the imaginary component of the induced voltage. The effects of rotating shaft materials and the magnetic gap between coils and the rotating part on eddy current speed sensor were investigated, which are important factors on sensor accuracy and sensitivity. Using copper disc also suppresses the effect of the shaft material. A 2D approximate analytical method was utilized for fast parametric analysis of the eddy current sensor. 3D time-stepping FEM with taking into account shaft rotating speed was used for detailed and more precise analysis of the sensor performance and comparison with measurements. The real component of induced voltage in the antiserially connected pick up coils is correlated to the eddy current losses in the moving part and the imaginary component of voltage represents the inductive coupling between the excitation coil and pick up coils.

Optimizations of axial airgap eddy current speed sensors are planned for future works in terms of increasing sensitivity and improving nonlinearity errors using optimum shape and dimensions for copper disc and choosing best nonmagnetic materials, for example, between aluminum with different conductivities, brass or stainless steel, for it. We will also concentrate on the compensation of temperature effects on material properties and airgap. Operating and evaluating axial airgap eddy current speed sensor at higher speeds are also considered for further developments.

APPENDIX

The 3D model of the eddy current sensor is simplified to a linearized 2D model as it is a common method to analyze axial airgap induction machines [35] - [36]. Equation (2) presents differential equations for 7 regions as shown in Fig. 24. A_z is a magnetic vector potential.
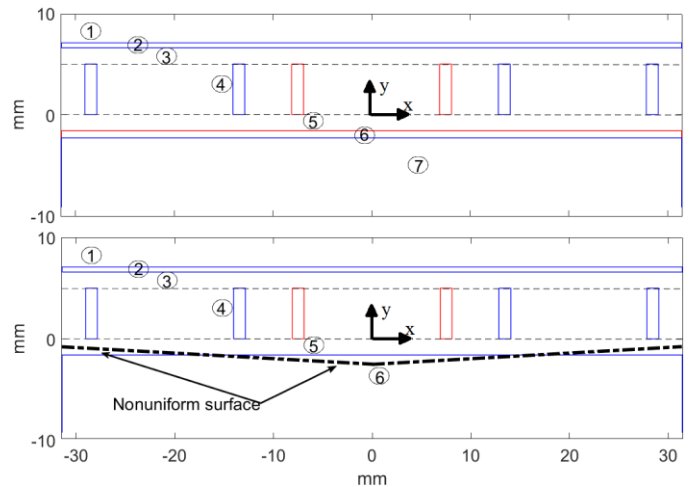

Fig. 24. 2D linearized model of axial airgap eddy current speed sensor for the analytical analysis
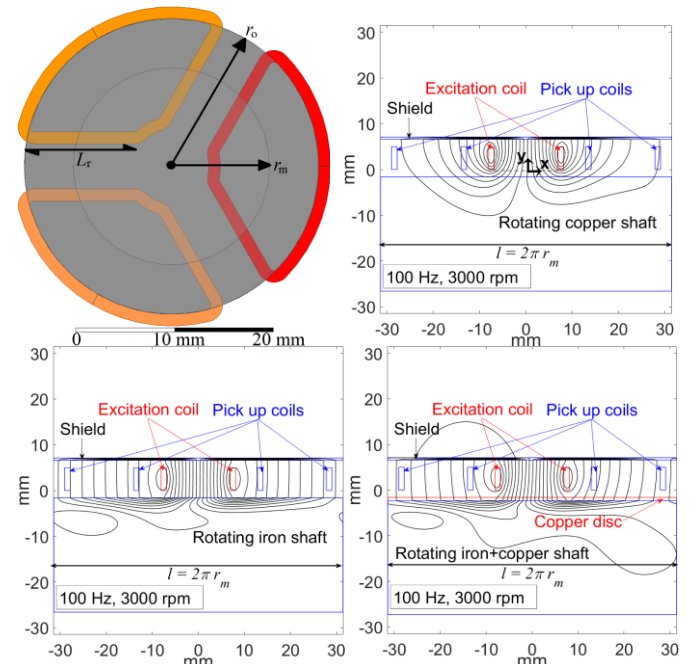

Fig. 25. 2D in-plane view of coils and rotating shaft and magnetic flux distribution with rotating copper shaft, iron shaft, and iron shaft+copper disc

Regions 1, 2, 3, 4, 5, 6 and 7 correspond to parts above shield, shield, air gap between shield and coils, coils, the air gap between coils and shaft, copper disc and solid iron shaft, respectively. In the case of no copper disc, it will be only 6 regions and region 6 is an only copper or an only iron shaft.

$$\frac{\partial^2 A_{z,1}}{\partial x^2} + \frac{\partial^2 A_{z,1}}{\partial y^2} = 0$$

$$\frac{\partial^2 A_{z,2}}{\partial x^2} + \frac{\partial^2 A_{z,2}}{\partial y^2} = j\omega\sigma_s\mu_0\mu_{r,s}A_{z,2}$$

$$\frac{\partial^2 A_{z,3}}{\partial x^2} + \frac{\partial^2 A_{z,3}}{\partial y^2} = 0$$

$$\frac{\partial^2 A_{z,4}}{\partial x^2} + \frac{\partial^2 A_{z,4}}{\partial y^2} = -\mu_0 J_s$$

$$\frac{\partial^2 A_{z,5}}{\partial x^2} + \frac{\partial^2 A_{z,5}}{\partial y^2} = 0$$

$$\frac{\partial^2 A_{z,6}}{\partial x^2} + \frac{\partial^2 A_{z,6}}{\partial y^2} = \sigma_c' \mu_0 \left(j\omega A_{z,6} + V\frac{\partial A_{z,6}}{\partial x} \right)$$

$$\frac{\partial^2 A_{z,7}}{\partial x^2} + \frac{\partial^2 A_{z,7}}{\partial y^2} = \sigma_i' \mu_0 \mu_{r,i} \left(j\omega A_{z,7} + V\frac{\partial A_{z,7}}{\partial x} \right)$$

(2)

The solutions of (2) are obtained using the separation of variables (Fourier method) [37]:

$$A_{z,1} = \sum_{n=\pm1,\pm2,\cdots} \left(C_{1,1}e^{\gamma y} + C_{2,1}e^{-\gamma y} \right) e^{j(\omega t - mx)}$$

$$m = \frac{2\pi n}{l}, \qquad l = 2\pi r_m, \quad \gamma = |m|$$

$$A_{z,2} = \sum_{n=\pm1,\pm2,\cdots} \left(C_{1,2}e^{\lambda_s y} + C_{2,2}e^{-\lambda_s y} \right) e^{j(\omega t - mx)}$$

$$\lambda_s = \sqrt{m^2 + j\omega\sigma_s\mu_0\mu_{r,s}}$$

$$A_{z,3} = \sum_{n=\pm1,\pm2,\cdots} \left(C_{1,3}e^{\gamma y} + C_{2,3}e^{-\gamma y} \right) e^{j(\omega t - mx)}$$

$$A_{z,4} = \sum_{n=\pm1,\pm2,\cdots} \left(C_{1,4}e^{\gamma y} + C_{2,4}e^{-\gamma y} + \frac{\mu_0 J_{s,n}}{m^2} \right) e^{j(\omega t - mx)}$$

$$J_{s,n} = \frac{J_s}{jn\pi} \left(\cos(m(0.5w_c + t_c)) - \cos(mt_c) \right), \quad J_s = \frac{N_e I}{h_c t_c}$$

$$A_{z,5} = \sum_{n=\pm1,\pm2,\cdots} \left(C_{1,5}e^{\gamma y} + C_{2,5}e^{-\gamma y} \right) e^{j(\omega t - mx)}$$

$$A_{z,6} = \sum_{n=\pm1,\pm2,\cdots} \left(C_{1,6}e^{\lambda_c y} + C_{2,6}e^{-\lambda_c y} \right) e^{j(\omega t - mx)}$$

$$\gamma_c = \sqrt{m^2 + j\sigma_c'\mu_0(\omega - mV)}, \quad V = r_m \cdot n_r$$

$$A_{z,7} = \sum_{n=\pm1,\pm2,\cdots} \left(C_{1,7}e^{\lambda_i y} + C_{2,7}e^{-\lambda_i y} \right) e^{j(\omega t - mx)}$$

$$\gamma_i = \sqrt{m^2 + j\sigma_i'\mu_0\mu_{r,i}(\omega - mV)}, \quad V = r_m \cdot n_r$$

(3)

To obtain constants, C_1's and C_2's in (3), boundary conditions between regions in (3) are applied. H_x and B_y are x-component of magnetic field strength and y-component of magnetic flux density (Fig. 25), respectively. All dimensional parameters in (2)-(4) are explained in Table I. $\mu_{r,s}$ and $\mu_{r,i}$ are relative magnetic permeability of shield and solid iron shaft. σ_c' and σ_i' are modified or effective copper disc and solid iron and copper shaft conductivities using (5) with considering the third dimension using Russel-Northworthy factor [38], respectively. n_r is the rotating speed of the shaft.

$$A_{z,1} = 0 \big| (y = \infty)$$
$$H_{x,1} = H_{x,2} \big| (y = h_c + g_s + h_s)$$
$$B_{y,1} = B_{y,2} \big| (y = h_c + g_s + h_s)$$
$$H_{x,2} = H_{x,3} \big| (y = h_c + g_s)$$
$$B_{y,2} = B_{y,3} \big| (y = h_c + g_s)$$
$$H_{x,3} = H_{x,4} \big| (y = h_c)$$
$$B_{y,3} = B_{y,4} \big| (y = h_c)$$

$$H_{x,4} = H_{x,5} \big| (y = 0)$$
$$B_{y,4} = B_{y,5} \big| (y = 0)$$
$$H_{x,5} = H_{x,6} \big| (y = -g_m)$$
$$B_{y,5} = B_{y,6} \big| (y = -g_m)$$
$$H_{x,6} = H_{x,7} \big| (y = -g_m - h_d)$$
$$B_{y,6} = B_{y,7} \big| (y = -g_m - h_d)$$
$$A_{z,7} = 0 \big| (y = -\infty)$$

(4)

$$\sigma_i' = k_{R-N}\sigma_i, \quad \sigma_c' = k_{R-N}\sigma_c$$

$$k_{R-N} = 1 - \frac{\tanh\left(\frac{\pi}{\tau}\frac{L_r}{2}\right)}{\left(\frac{\pi}{\tau}\frac{L_r}{2}\right)\left(1 + \tanh\left(\frac{\pi}{\tau}\frac{L_r}{2}\right)\tanh\left(\frac{\pi}{\tau}\frac{w_o}{2}\right)\right)}, \tau = \frac{l}{3|n|}$$

(5)

where, w_o (copper disc overhang) in (5) is r_d-r_o to calculate k_{R-N} for copper disc according to Table I. It is zero for only iron or copper shaft or when copper disc has the same diameter as the rotating shaft.

Fig. 25 shows the 2D view of coils and magnetic flux distribution with an only copper shaft, an only solid iron shaft, and solid iron shaft with the copper disc. Equation (6) presents differential induced voltage, $U_{p,d}$ in antiserially connected pick up coils [29].

$$U_{p,r} = -2\omega N_p L_r \sum_{n=\pm1,\pm2,\cdots} C_{U,1} \cdot C_{U,2} \, e^{-j\frac{2n\pi}{3}} e^{j\omega t}$$

$$C_{U,1} = \frac{\left(\cos(m \cdot (0.5w_c + t_c)) - \cos(m \cdot 0.5w_c)\right)}{mh_c t_c}$$

$$C_{U,2} = \left(C_{1,4}\frac{(e^{\gamma h_c} - 1)}{\gamma} - C_{2,4}\frac{(e^{-\gamma h_c} - 1)}{\gamma} + \frac{\mu_0 J_{s,n}}{m^2}h_c \right)$$

$$U_{p,l} = -2\omega N_p L_r \sum_{n=\pm1,\pm2,\cdots} C_{U,1} \cdot C_{U,2} \, e^{j\frac{2n\pi}{3}} e^{j\omega t}$$

$$U_{p,d} = U_{p,l} - U_{p,r}$$

$$= -j4\omega N_p L_r \sum_{n=\pm1,\pm2,\cdots} C_{U,1}$$

$$\cdot C_{U,2} \sin\left(\frac{2n\pi}{3}\right) e^{j\omega t}$$

(6)

The emf of the excitation coil in (7) could be calculated as (6) and the results are shown in Fig. 26 for the real and imaginary components. The speed has small effect on the excitation coil emf, especially for the imaginary component.

$$U_e = -2\omega N_e L_r \sum_{n=\pm1,\pm3,\cdots} C_{U,1} \cdot C_{U,2} \, e^{j\omega t}$$
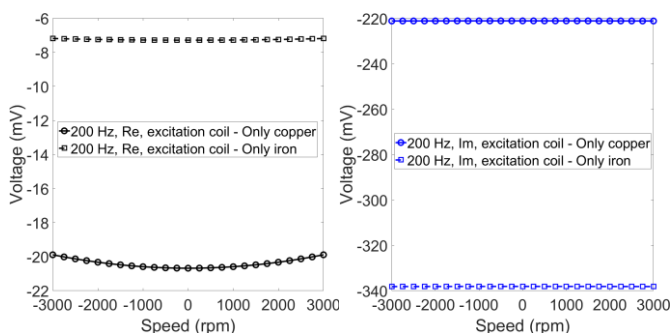
(7)

Fig. 26. Real (Re) and imaginary (Im) components of emf of the excitation coil

REFERENCES

[1] I. Boldea, A. Rahman, S. A. Nasar, "Finite-width, finite-thickness, and saturation effects in solid-rotor induction machines," *IEEE Trans. Power App. Sys.*, vol. 94, no. 5, pp. 1500-1507, Sep./Oct. 1975

[2] P.D. Evans, J.F. Eastham, "Segmented-rotor disc motor," *IEE J. Elec. Power App.*, vol. 1, no. 1, pp. 7-16, Feb. 1978

[3] P.D. Evans, J.F. Eastham, "Disc-geometry homopolar synchronous machine," *IEE Proc. B - Elec. Power App.*, vol. 127, no. 5, pp. 299-307, Sept. 1980

[4] Z. Zhang, C. Wang, and W. Geng, "Design and optimization of Halbach-array PM rotor for high-speed axial-flux permanent magnet machine with ironless stator," *IEEE Trans. Ind. Elec.,* vol. 67, no. 9, pp. 7269-7279, Sept. 2020

[5] M. Noh and D. L. Trumper, "Homopolar bearingless slice motor with flux-biasing Halbach arrays," *IEEE Trans. Ind. Elec.,* vol. 67, no. 9, pp. 7757-7766, Sept. 2020

[6] C. Gong, S. Li, T. Habetler, J. A. Restrepo, and B. Soderholm, "Direct position control for ultrahigh-speed switched-reluctance machines based on low-cost nonintrusive reflective sensors," *IEEE Trans. Ind. Appl.*, vol. 55, no. 1, pp. 480–489, Jan./Feb. 2019

[7] Y. Wang, C. Wu, and S. Yang, "A self-powered rotating speed sensor for downhole motor based on triboelectric nanogenerator," *IEEE Sens. J.*, vol. 21, no. 4, pp. 4310–4316, Feb. 2021

[8] J. Guzinski and H. Abu-Rub, "Speed sensorless induction motor drive with predictive current controller," *IEEE Trans. Ind. Elec.*, vol. 60, no. 2, pp. 699-709, Feb. 2013

[9] Z. Zhang, F. Ni, Y. Dong, C. Guo, M. Jin, and H. Liu, "A novel absolute magnetic rotary sensor," *IEEE Trans. Ind. Electron.*, vol. 62, no. 7, pp. 4408–4419, Jul. 2015

[10] L. Sun, J. Taylor, A. D. Callegaro, and A. Emadi, "Stator-PM-based variable reluctance resolver with advantage of motional back-EMF," *IEEE Trans. Ind. Electronics.* vol. 67, no. 11, pp. 9790-9801, Nov. 2020

[11] S. Chen, Y. Zhao, H. Qiu , and X. Ren, "High-precision rotor position correction strategy for high-speed permanent magnet synchronous motor based on resolver," *IEEE Trans. Pow. Elect.*, vol. 35, no. 9, pp. 9716-9726, Sept. 2020

[12] L. Sun, Z. Luo, K. Wang, R. Cao, and S. Ding, "A stator-PM resolver with field modulation principle," *IEEE Trans. Energ. Conv.*, 2020 (Early access)

[13] T. Addabbo *et al.*, "Instantaneous rotation speed measurement system based on variable reluctance sensors for torsional vibration monitoring," *IEEE Trans. Instrum. Meas.*, vol. 68, no. 7, pp. 2363–2373, Jul. 2019

[14] H. Saneie, Z. Nasiri-Gheidari, and F. Tootoonchian, "Design-oriented modelling of axial-flux variable-reluctance resolver based on magnetic equivalent circuits and Schwarz–Christoffel mapping," *IEEE Trans. Ind. Electron.*, vol. 65, no. 5, pp. 4322–4330, May 2018

[15] C. Gong, A. Tuysuz, M. Flankl, T. Stolz, J. Kolar, T. Habetler, "Experimental analysis and optimization of a contactless eddy-current-based speed sensor for smooth conductive surfaces," *IEEE Trans. Ind. Elect.*, vol. 67, no. 10, pp. 8817-8828, Oct. 2020

[16] J. Wang and J. Zhu, "A simple method for performance prediction of permanent magnet eddy current couplings using a new magnetic equivalent circuit model," *IEEE Trans. Ind. Electron.*, vol. 65, no. 3, pp. 2487–2495, Mar. 2018

[17] X. Liu, C. Liu, and P. W. T. Pong, "Velocity measurement technique for permanent magnet synchronous motors through external stray magnetic field sensing," *IEEE Sensors J.*, vol. 18, no. 10, pp. 4013-4021, May 15, 2018

[18] V. Petrucha and P. Ripka, "Rotational speed measurement and angular position reference for a cryogenic propellant electric pump," *J. of Elec. Eng.*, vol. 66, no. 7/s, pp. 199-202, 2015

[19] J.A. Shercliff, *The Theory of Electromagnetic Flow Measurement*, Cambridge University Press, 1962.

[20] C. C. Feng, W. E. Deeds, C. V. Dodd, "Analysis of eddy-current flowmeters," *J. Appl. Phys.,* vol. 46, no. 7, pp. 2935-2940, 1975

[21] N. Takehira, A. Tanaka, K. Toda, "Analysis of a speed-meter utilizing eddy current effect," *The trans. Inst. Elect. Eng. Japan. A,* vol. 97, no. 9, pp. 457-464, Sept. 1977

[22] N. Takehira, A. Tanaka, "Analysis of a transmitted type speed-meter utilizing eddy current effect," *The trans. Inst. Elect. Eng. Japan. A,* vol. 100, no. 9, pp. 483-490, Sept. 1980

[23] A. Tanaka, N. Takehira, "Eddy-current speed meter using Galvanomagnetic devices," *The trans. Inst. Elect. Eng. Japan. A,* vol. 106, no. 6, pp. 267-274, June 1986

[24] K. Ishida, T. Itaya T, A. Tanaka A, N. Takehira, "Exact analysis of a linear velocity sensor," *IEEE Trans. on Inst. and Meas.,* 2020 (Early access).

[25] M. Mirzaei, P. Ripka, J. Vyhnanek, A. Chirtsov and V. Grim, "Rotational eddy current speed sensor," *IEEE Trans. Mag.*, vol. 55, no. 9, 4003710, September 2019

[26] M. Mirzaei, P. Ripka, V. Grim, and A. Chirtsov, "Design and optimization of an eddy current speed sensor for rotating rods," *IEEE Sens. J.*, vol. 20, no. 20, pp. 12241-12251, June 2020

[27] Axial airgap motors, http://www.atb motors.com/uploads/03_PRODUK TE_Axialspaltmotoren_182_DE.pdf, Accessed on 04.06.2021 [Online]

[28] J. Mei, Y. Zuo, C. H. T. Lee, and J. L. Kirtley, "Modeling and optimizing method for axial flux induction motor of electric vehicles," *IEEE Trans. Veh. Tech.*, vol. 69, no. 11, pp. 12822-12831, Nov. 2020

[29] P. Zhou, Z. Badics, D. Lin, and Z. J. Cendes, "Nonlinear T-Ω formulation including motion for multiply connected 3-D problems," *IEEE Trans. Mag.*, vol. 44, no. 6, pp. 718-721, June 2008.

[30] Ansys/maxwell (Ansoft), https://www.ansys.com/products/electronics/a nsys-maxwell, Accessed on 04.06.2021 [Online]

[31] E. Cardelli, A. Faba, and F. Tissi, "Contact-less speed probe based on eddy currents," *IEEE Trans. Magn.*, vol. 49, no. 7, pp. 3897–3900, Jul. 2013.

[32] T. Sonoda, R. Ueda, K. Fujitani, T. Irisa, and S. Tatata, "DC magnetic field type eddy current speed sensor detecting cross magnetization field with amorphous core," *IEEE Trans. Magn.*, vol. MAG-21, no. 5, pp. 1732–1734, Sep. 1985.

[33] Handheld Tachometer, https://www.onosokki.co.jp/English/hp_e/whats_ new/Catalog/PDF/ht5500e.pdf, Accessed on 04.06.2021 [Online]

[34] M. Lu, W. Zhu, L. Yin, A. J. Peyton, W. Yin, and Z. Qu, "Reducing the lift-off effect on permeability measurement for magnetic plates from multifrequency induction data," *IEEE Trans. Instr. & Meas.*, vol. 67, no. 1, pp. 167-174, Jan. 2018.

[35] E. Mendrela, J. Fleszar and E. Gierczak, *Modeling of Induction Motors with One and Two Degrees of Mechanical Freedom*, Springer Science+Business Media, LLC, 2003

[36] C. Hong, W. Huang, and Z. Hu, "Performance calculation of a dual stator solid rotor axial flux induction motor using the multi-slice and multi-layer method," *IEEE Trans. Mag.*, vol. 55, no. 2, 8100709, Feb. 2019

[37] M. Mirzaei, P. Ripka, A. Chirtsov, J. Vyhnanek, and V. Grim, "Design and modeling of a linear speed sensor with a flat type structure and air coils," *J. of Magnetism and Magnetic Materials*, vol. 495, 165834, 2020

[38] J. F. Gieras, and J. Saari, "Performance calculation for a high-speed solid-rotor induction motor," *IEEE Trans. Ind. Elec.*, vol. 59, no. 6, pp. 2689-2700, June 2012

Mehran Mirzaei is a postdoc researcher in the Department of Measurement, Faculty of Electrical Engineering, Czech Technical University, Prague, Czech Republic. He analyzes and optimizes magnetic position sensors and eddy current speed sensors. His research topic is magnetic material modeling in magnetic sensors and transducers.

Pavel Ripka received the Ing. degree in electrical engineering and the C.Sc. degree (equivalent to PhD) in 1984 and 1989, respectively, and the Docent degree in 1996. Since 2001, he has been a Full Professor with Czech Technical University. He is the coauthor of three books and

150 journal articles. His main research interests are magnetic measurements and magnetic sensors, especially fluxgate.

Vaclav Grim is currently pursuing the PhD degree with the Department of Measurement, Faculty of Electrical Engineering, Czech Technical University, Prague, Czech Republic. He works on applications of magnetic sensors, characterization, and optimization. His research topic is optimization of magnetic sensors.